Advanced Functional Materials

ADVANCED FUNCTIONAL MATERIALS
www.afm-journal.de

RESEARCH ARTICLE

Anion-Position-Driven Photoluminescence Enhancement Enables Low-Threshold Lasing in $CsPbCl_xBr_{3\text{-}x}$ Microwires

Dahai Cheng[1] | Long Yuan[2,3] | Qiushi Yao[1] | Wenjie Deng[1] | Yanda Ji[1] | Caixia Kan[1] | Caofeng Pan[2,3] | Junfeng Lu[1]

[1]College of Physics Nanjing University of Aeronautics and Astronautics Nanjing, P. R. China | [2]Institute of Atomic Manufacturing, Beihang University, Beijing, P. R. China | [3]Beijing Key Laboratory for Atomic Manufacturing Equipment and Intelligent Sensing, Beijing, China

Correspondence: Qiushi Yao (yaoqiushi@nuaa.edu.cn) | Caofeng Pan (pancaofeng@buaa.edu.cn) | Junfeng Lu (lujunfeng@nuaa.edu.cn)

Received: 10 November 2025 | **Revised:** 22 March 2026 | **Accepted:** 27 April 2026

Keywords: anion exchange | high-temperature annealing | lattice engineering | perovskite lasers

ABSTRACT

Cesium lead halide perovskites ($CsPbX_3$) have emerged as promising materials for optoelectronic applications due to their excellent solution processability, tunable broadband bandgap, and superior charge carrier transport properties. However, bandgap tunability is typically achieved through halide ion exchange, which often introduces defects, leading to decreased luminescence efficiency and limiting practical applications. Here, we demonstrate anion-position-driven lattice reconfiguration strategy as a simple yet effective strategy to optimize the optical properties of perovskite alloy microwires. The PL intensity increases by 2–3 orders of magnitude, demonstrating exceptional stimulated emission characteristics. Theoretical simulations, supported by temperature-dependent photoluminescence (PL) spectroscopy, reveal that halide ion migration during annealing facilitates defect passivation, significantly enhancing radiative recombination efficiency. Additionally, the lasing threshold of the annealed alloy microwires decreases dramatically from an initial 62.82 to 11.8 μJ/cm^2, representing an over 80% reduction. This study highlights the critical role of high-temperature annealing in optimizing the optoelectronic properties of perovskites and underscores its potential for enabling low-threshold, high-efficiency perovskite micro-lasers for next-generation photonic devices.

1 | Introduction

Lead halide perovskites (LHPs) have rapidly emerged as a research focus in optoelectronics and photonics due to their unique crystal structure and outstanding optoelectronic properties. These materials exhibit exceptional photoluminescence quantum efficiency [1, 2], high charge carrier mobility, tunable broadband bandgap [3–10]and long carrier lifetimes [11, 12], making them highly promising for applications in light-emitting diodes (LEDs) [13–18], photodetectors [19–28], solar cells [29, 30], and low-threshold lasers [31–35]. Among them, cesium lead halide perovskites ($CsPbX_3$, X = Cl, Br, I) have garnered significant interest as a representative class of all-inorganic perovskites, owing to their superior thermal stability and environmental robustness. These properties render them highly advantageous for the design and fabrication of micro/nano-photonics devices [36, 37].

Furthermore, owing to its soft-lattice structural characteristics [38], anion exchange has been widely employed as an effective strategy for bandgap tuning [39–41]. For instance, Lu synthesized a $CsPbCl_xBr_{3\text{-}x}$ perovskite microwire with a continuously tunable bandgap gradient ranging from 2.33 to 2.83 eV along its axial direction using a vapor-phase anion exchange method, thereby realizing a continuously tunable single-mode laser [7]. Li et al. fabricated $CsPbCl_xBr_{3\text{-}x}$ ($0< x < 2$) microwire alloys via a vapor-phase anion exchange method, achieving wavelength-tunable single-mode lasing from 546.8 to 468.0 nm [39]. Fu successfully fabricated compositionally tunable perovskite nanowires via a vapor-phase halide anion exchange reaction, achieving broadband wavelength-tunable lasing emission spanning from 420 to 710 nm [42]. Despite the tremendous potential of $CsPbX_3$ materials in the field of wavelength tunable lasers, achieving high-quality $CsPbCl_xBr_{3-x}$ alloyed perovskite microwires remains a significant technological challenge. These challenges primarily stem from non-radiative recombination centers and surface defects, which limit both luminescence efficiency and optical gain. Particularly, these anion exchange processes inherently rely on ion interdiffusion, inevitably introducing point defects and halide vacancies. These defects act as non-radiative recombination centers, significantly suppressing the photoluminescence efficiency of perovskite alloys [9, 43, 44]. Therefore, the development of effective post-treatment strategies to mitigate defect formation and enhance the optical properties of $CsPbX_3$ materials is of critical importance.

Here, we successfully synthesized high-quality $CsPbCl_xBr_{3-x}$ microwires using an anion-position-driven lattice engineering strategy and systematically investigated the impact of halide exchange and intrinsic lattice reconfiguration on their optical properties and lasing characteristics via first-principles calculations. Distinct from conventional thermal treatments that focus on extrinsic morphology optimization, this strategy identifies high-temperature annealing as a vital kinetic pathway to relocate halide ions from disordered, high-energy interstitial sites inherent to the vapor-phase exchange process back to their thermodynamically stable, regular lattice positions. First-principles calculations validate the energetic favorability of this lattice reconfiguration, providing a theoretical foundation for the transition from a defect-dominated state to a stable excitonic state as anions occupy their thermodynamic equilibrium positions. Experimental results show that after annealing, the photoluminescence intensity is significantly enhanced by two to three orders of magnitude. Simultaneously, the lasing threshold is substantially reduced, demonstrating excellent optical gain performance. This study not only highlights the crucial role of anion-position-driven lattice engineering strategy in optimizing the optical properties of perovskite micro- and nanostructures but also provides valuable insights for their application in low-threshold lasers and high-performance photonic devices.

2 | Results and Discussion

To prepare the $CsPbCl_xBr_{3-x}$ perovskite microwires, $CsPbBr_3$ microwires were first fabricated using a solution-based method. Figure 1a displays a typical scanning electron microscope (SEM) image of a $CsPbBr_3$ microwire with a width of 4.8 μm, including both the overall morphology and a localized view of the central region. The inset in the lower-right corner shows a fluorescence mapping image of an individual $CsPbBr_3$ microwire. (Additional SEM and fluorescence mapping images of the microwire's tip and larger regions are provided in Figure S1). The smooth surface and rectangular cross-section of the microwire suggest that it can function as a natural optical resonator, supporting whispering-gallery mode (WGM) oscillations by enabling full internal light confinement and total internal reflection along its four inner walls. Figure 1b presents the energy dispersive X-ray spectroscopy (EDS) map of Cs, Pb, and Br elements at the tip of the microwire, confirming the uniform distribution of elements throughout the microwire. The structure of the microwire was further characterized by X-ray diffraction (XRD) analysis, as shown in Figure 1c. The XRD results indicate that the $CsPbBr_3$ microwires possess an orthorhombic phase (space group *Pbnm*), consistent with ICSD #97851. Six primary diffraction peaks are observed at 15.03°, 15.19°, 21.44°, 21.62°, 30.35°, and 30.68°, corresponding to the (002), (110), (112), (200), (004), and (220) crystal planes, respectively. Additionally, the characteristic splitting of diffraction peaks near 15° and 30° further confirms the presence of the orthorhombic phase at room temperature. Steady-state photoluminescence (PL) and absorption spectra of an individual $CsPbBr_3$ microwire were also measured and are shown in Figure 1d. A strong spontaneous emission peak at 524 nm was observed, aligning with the absorption edge, which indicates that the emission arises from intrinsic radiative recombination between conduction band electrons and valence band holes. Notably, a weak excitonic absorption peak is observed near the absorption edge at room temperature, which is attributed to the bound exciton states in the material. As illustrated in the figures, the excitonic features are scarcely discernible to the naked eye due to the significantly attenuated absorption at the band edge.

The $CsPbBr_3$ perovskite microwires were fabricated using a Vapor-phase halide exchange method to obtain $CsPbCl_xBr_{3-x}$ perovskite microwires. As shown in Figure 2a, the vapor-phase halogen exchange system was designed to ensure a controlled exchange environment. Anhydrous calcium chloride pellets were placed in the petri dish to act as a desiccant, absorbing the water vapor evaporated from the concentrated HCl solution. This ensured a dry reaction environment, which is critical to preventing moisture-induced degradation of the perovskite microwires while allowing the gaseous HCl to facilitate the anion exchange process. To verify the wide applicability of the vapor-phase anion exchange method, Figure 2b presents the X-ray diffraction (XRD) patterns, revealing significant structural changes in the perovskite microwires before and after exchange. The original $CsPbBr_3$ microwires exhibited two main diffraction peaks at 15.20° and 30.68°, corresponding to the (110) and (220) planes of the orthorhombic perovskite structure (space group *Pbnm*). Additionally, the noticeable splitting of the (002) and (110) diffraction peaks further confirmed the tilting and distortion of the PbX_6 octahedra at room temperature. After a 6 h chloride ion exchange, the (110) and (220) diffraction peaks significantly shifted to 15.44° and 31.18°, respectively. This peak shift indicates the successful incorporation of Cl^-, and leading to a reduction in lattice spacing as per Bragg's law ($2d\sin\theta = n\lambda$). To quantitatively justify the lattice contraction, the lattice parameters were extracted from the XRD patterns. For the (110) plane, the 2θ angle shifted from 15.186° to 15.448°, corresponding to a decrease in the interplanar d-spacing from 5.8294 to 5.7313 Å. Similarly, the d-spacing for the (220) plane reduced from 2.9118 to 2.8662 Å. These results provide conclusive evidence of structural contraction following the incorporation of smaller Cl^- ions into the $CsPbBr_3$ framework. Furthermore, the introduction of Cl^- resulted in lattice distortion or additional crystal defects, such as dislocations or vacancies, which introduce non-radiative recombination centers, causing the excited electrons and holes to dissipate through non-radiative pathways and reducing the PL intensity. These findings suggest that vapor-phase anion

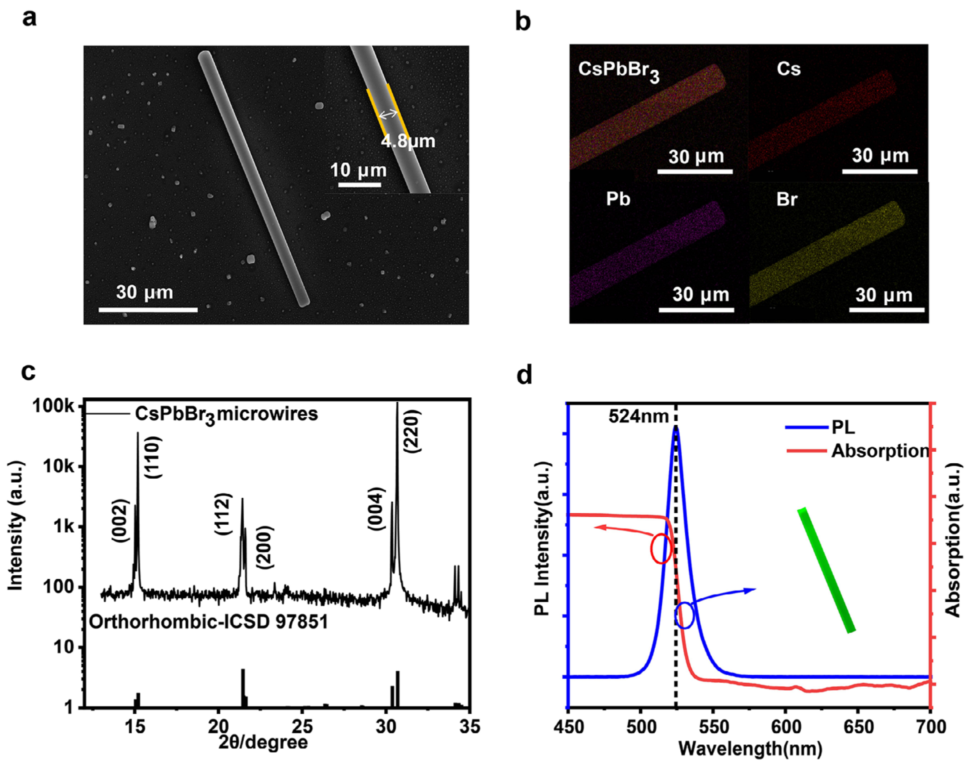

FIGURE 1 | Morphological, structural, and optical characterization. (a) Scanning electron microscope (SEM) image of a single $CsPbBr_3$ microwire. (b) Energy dispersive X-ray spectroscopy (EDS) elemental mapping of a single $CsPbBr_3$ perovskite microwire. (c) X-ray diffraction (XRD) pattern of orthorhombic-phase $CsPbBr_3$ microwire, compared with the standard reference (ICSD #97851). (d) Steady-state micro-photoluminescence (μ-PL) and absorption spectra of a single $CsPbBr_3$ perovskite microwire, with the fluorescence mapping of a single $CsPbBr_3$ perovskite microwire shown in the lower-right inset.

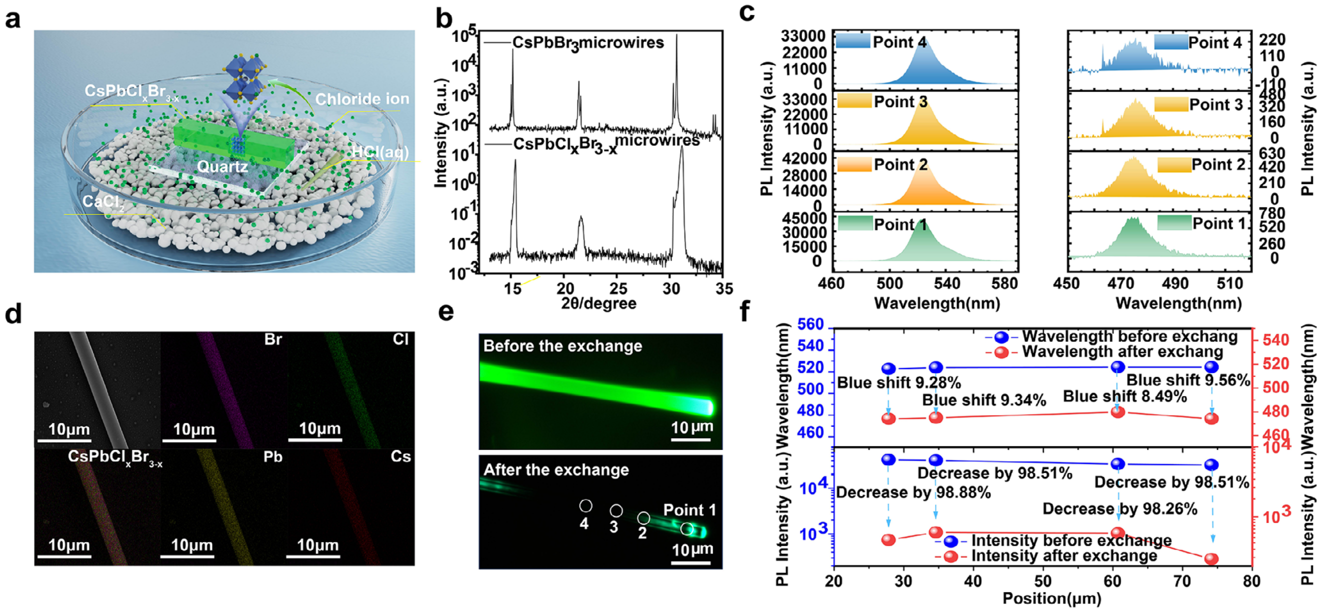

FIGURE 2 | Device structure, elemental, and optical characterization. (a) Schematic diagram of the vapor-phase halogen exchange system used. (b) X-ray diffraction (XRD) pattern of $CsPbCl_xBr_{3-x}$ perovskite microwires. (c) Photoluminescence (PL) intensity of a single $CsPbBr_3$ perovskite microwire before (left) and after (right) halogen exchange. (d) Scanning electron microscope (SEM) image and energy dispersive X-ray spectroscopy (EDS) elemental mapping of a single $CsPbCl_xBr_{3-x}$ perovskite alloy microwire. (e) Photoluminescence (PL) mapping of a single $CsPbBr_3$ perovskite microwire before and after halogen exchange. (f) Changes in the photoluminescence (PL) center wavelength and intensity at different locations on the $CsPbBr_3$ perovskite microwire before and after halogen exchange.

exchange not only effectively tunes the composition of the perovskite alloy but also profoundly impacts its crystal structure.

Energy dispersive X-ray spectroscopy (EDS) was used to analyze the elemental distribution in a single $CsPbCl_xBr_{3-x}$ microwire (Figure 2d), which revealed a uniform distribution of Cl, Br, Cs, and Pb, confirming the successful incorporation of halogens during the exchange process. The quantitative elemental compositions and the corresponding stoichiometric ratios are detailed in Figure S3. Photoluminescence (PL) spectra further revealed changes in the optical properties of a single microwire before and after halogen exchange. As shown in Figure 2c, the PL spectra at four different locations along the microwire exhibited shifts in the PL center wavelength and intensity, reflecting significant changes in composition and optical performance. PL mapping (Figure 2e) revealed a pronounced blueshift in the emission wavelength across nearly the entire microwire after halogen exchange, indicating an effective enlargement of the bandgap of $CsPbCl_xBr_{3-x}$ compared to pristine $CsPbBr_3$, which is further confirmed by our first-principles calculations. As shown in Figure S2c, the calculated bandgap of pristine $CsPbBr_3$ is 2.112 eV. While for $CsPbCl_{0.25}Br_{2.75}$ (x = 0.25), the calculated bandgap increased to 2.148 eV (Figure S2d), in agreement with the blueshift of PL spectra. (It should be noted that we selected $x = 0.25$ as a representative composition and employed DFT at the GGA-PBE level (which tends to underestimate the bandgap). Therefore, the calculated results are intended to qualitatively explain the bandgap enlargement and PL blueshift induced by halide substitution, and are not strictly quantitative.) Bandgap of $CsPbCl_xBr_{3-x}$ behaves in a monotonic way as a function of x [7]. (Note that while the 450 nm light effectively excites the material, the resulting PL emission near 470 nm could no longer be captured by the fluorescence imaging system due to the cutoff of the optical filters used to block the excitation source. This, combined with the decreased luminescence efficiency caused by exchange-induced defects, results in the microwire appearing black in the mapping images. However, the actual emission remains clearly detectable via spectroscopic measurements (as shown in Figure 2c,f), which utilize a spectrometer to resolve the signal.). Bright-field optical images of $CsPbBr_3$ microwires before and after exchange are shown in Figure S2a,b. After chloride ion incorporation, Cl^- occupy the lattice interstitials, displacing Br^-, during the vapor-phase anion exchange process, the incorporation of Cl^- into the $CsPbBr_3$ lattice is not always uniform. In some cases, excessive Cl^- incorporation may occur, resulting in the simultaneous presence of both Cl^- and Br^-in lattice interstitial positions. This leads to lattice distortion and the formation of defect states near the band edge. These defect states act as nonradiative recombination centers, thereby reducing the effective carrier population available for optical gain, which is the main reason for the significant reduction in the emission intensity of the exchanged material. Furthermore, the non-uniform incorporation of Cl^- may lead to Cl^--rich regions on the surface of the microwires. These regions are unable to effectively passivate surface defects and instead introduce additional nonradiative recombination centers. In addition, the substitution of Br^- by the smaller Cl^- ions modifies the lattice parameters and induces localized tensile strain in the lattice due to lattice contraction. This strain further alters the carrier recombination pathways and increases the proportion of nonradiative recombination.

Figure 3a presents the PL spectra of a single $CsPbCl_xBr_{3-x}$ microwire at four different locations after various annealing times (30, 60, 90, 120, 150, and 180 min), revealing the influence of thermal treatment on the luminescent properties. Figure 3b further quantifies the evolution of PL intensity and center wavelength with respect to annealing time, showing that the PL intensity gradually increases as annealing time increases, while the emission peak exhibits a significant redshift during the initial stage (within 30 min) before stabilizing. This trend can be attributed to high-temperature annealing promoting long-range ordering of halide ions, reducing local strain, and lowering defect state density, thus minimizing non-radiative recombination pathways and enhancing luminescent efficiency.

The Cl^- introduced through ion exchange partially occupied the interstitial sites of the crystal, while simultaneously introducing interstitial Br^-. The subsequent annealing treatment facilitated the migration of interstitial Cl^- and Br^- back to lattice sites, repairing interstitial defects and improving the sample quality. Based on this picture, we investigated the evolution of the bandgap before and after annealing by using first-principles calculations. First, we identify three potential anion (Cl^- and Br^-) interstitial sites based on the spatial constraints of the crystal structure (Figure S4). By comparing the calculated bandgaps of $CsPbCl_xBr_{3-x}$ with anions occupying interstitial sites (before annealing) and lattice sites (after annealing), we systematically investigated the effects of annealing. On one hand, as shown in Figure 3e, for interstitial Br occupying sites 1 and 2, labeled as Br_i^1 and Br_i^2, annealing treatment induces a reduction of the bandgap, 14 meV for Br_i^1 and 8 meV for Br_i^2, respectively, in agreement with the experimentally observed redshift of PL peak. On the other hand, for Br_i^3, migration of interstitial Br to the lattice site leads to significant bandgap enlargement (85 meV), showing pronounced discrepancy with the experimental observations. However, energy of Br_i^3 is much higher than Br_i^1 and Br_i^2 (~ 30 meV/fu, Figure 3e), indicating that Br_i^3 is unstable. The composition of Br_i^3 would be extremely low, rendering its effects negligible. Thus, combining the calculated bandgaps and relatively energies, we conclude that stable Br_i^1 and Br_i^2 lead to bandgap reduction after annealing treatment, revealing the origin the PL redshift. For interstitial Cl^-, the above analysis remains equally applicable (Figure 3f). The light-emission performance of semiconductor materials is closely associated with exciton-phonon scattering and exciton binding energy. The former, often related to defect states, serves as a non-radiative decay pathway for excitons, whereas the latter governs exciton stability under thermal perturbation. A higher exciton binding energy facilitates the formation of stable excitons and promotes radiative recombination, thereby enabling a higher photoluminescence quantum yield (PLQY) [45]. To quantitatively evaluate the emission efficiency, the PLQY was measured using an integrating sphere (Figure S5). The PLQY exhibits a remarkable 35-fold increase from 0.01 to 0.35 following the high-temperature annealing process. Although the absolute values are affected by the low coverage density of dispersed microwires within the macro-excitation spot (2 mm), the substantial relative enhancement directly correlates with the suppression of non-radiative traps and the restoration of a high-quality crystalline lattice.

To further investigate the impact of high-temperature annealing on the optical properties of perovskites, 2D photoluminescence

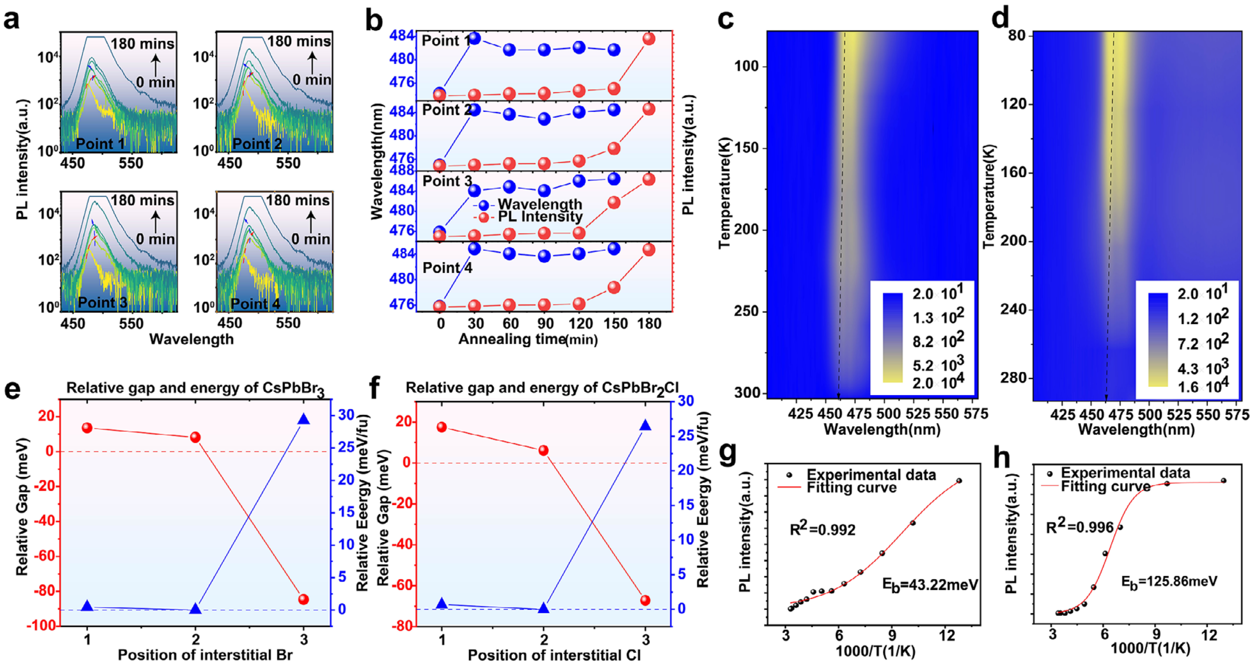

FIGURE 3 | High-temperature annealing enhances photoluminescence of $CsPbCl_xBr_{3-x}$ perovskite microwires. (a) Photoluminescence (PL) spectra of a single $CsPbCl_xBr_{3-x}$ perovskite microwire at four different locations after high-temperature annealing for 30, 60, 90, 120, 150, and 180 min. (b) Dependence of the PL intensity and center wavelength of a single $CsPbCl_xBr_{3-x}$ perovskite microwire on the annealing time. (c,d) 2D pseudo color images of a single $CsPbCl_xBr_{3-x}$ perovskite microwire at different temperatures (80–300 K) before (left) and after (right) annealing. (e,f) Calculated relative bandgaps and energies of $CsPbCl_xBr_{3-x}$ with anions occupying different interstitial sites. Bandgap reference is bandgap of $CsPbCl_xBr_{3-x}$ with anions occupying lattice sites, while energy reference is energy of $CsPbCl_xBr_{3-x}$ with anions occupying interstitial site 2. (g,h) Temperature dependence of the PL intensity before and after annealing.

(PL) spectral evolution of $CsPbCl_xBr_{3-x}$ microwires before and after annealing, in the temperature range of 80–300 K, is presented in Figure 3c,d. The temperature-dependent PL intensity maps reveal a pronounced and continuous blueshift of the emission peak, along with a broadening of the full width at half maximum (FWHM), observed consistently in both pre- and post-annealed samples. This blueshift of the PL peak with increasing temperature is primarily attributed to two interrelated mechanisms: lattice thermal expansion and exciton-phonon coupling [40, 45]. Thermal expansion modulates the Pb—X (X=Cl, Br) bond lengths, effectively altering the orbital overlap between the Pb 6p and halide np states. Such modifications influence the electronic band structure by narrowing the conduction band minimum (CBM) and shifting the valence band maximum (VBM), leading to an overall widening of the bandgap with temperature. Additionally, exciton-phonon interactions-particularly Fröhlich-type coupling, which is prominent in polar soft-lattice semiconductors such as lead halide perovskites-further contribute to this temperature-induced blueshift through phonon absorption and emission processes.

Electron-phonon interactions additionally contribute to this blueshift by renormalizing the band edges through phonon absorption and emission processes, with Fröhlich-type coupling playing a dominant role in polar soft-lattice semiconductors such as lead halide perovskites.

The temperature-dependent evolution of PL intensity is further quantitatively described by fitting to the Arrhenius equation, as follows [46]:

$$IT = \frac{I(0)}{1 + Cexp\left(E_b/KT\right)} \tag{1}$$

In the equation, I(0) represents the integral intensity at 0K, E_b is the exciton binding energy, K is the Boltzmann constant, and C is the relative contribution of non-radiative recombination. As shown in Figure 3 g,h, the exciton binding energy (E_b) extracted from the fitting curve after annealing increases from 43.22 to 125.86 meV, compared to pre-annealed samples. This value significantly exceeds the exciton binding energy (~40 meV) reported for $CsPbBr_3$ microwires and nanosheets synthesized via solution processing and chemical vapor deposition (CVD) epitaxial growth [40, 45, 47, 48]. The significant increase in exciton binding energy after annealing indicates a substantial reduction in defects and an improvement in crystallinity of the $CsPbCl_xBr_{3-x}$ microwires upon high-temperature treatment. As a result, the influence of thermal fluctuations on excitons is markedly suppressed. Under optical excitation, a larger number of excitons can be effectively generated, which accounts for the progressively enhanced photoluminescence (PL) intensity observed with increasing annealing time [13, 49]. This suggests that annealing significantly enhances the electron-hole binding interaction, enabling the material to retain strong exciton luminescence at higher temperatures. This result is crucial for the design of low-threshold perovskite lasers, as a higher exciton binding energy generally leads to stronger optical gain, lower lasing threshold, and superior high-temperature stability.

Moreover, the annealed samples exhibit stronger PL intensity across the entire temperature range, indicating that the reduction

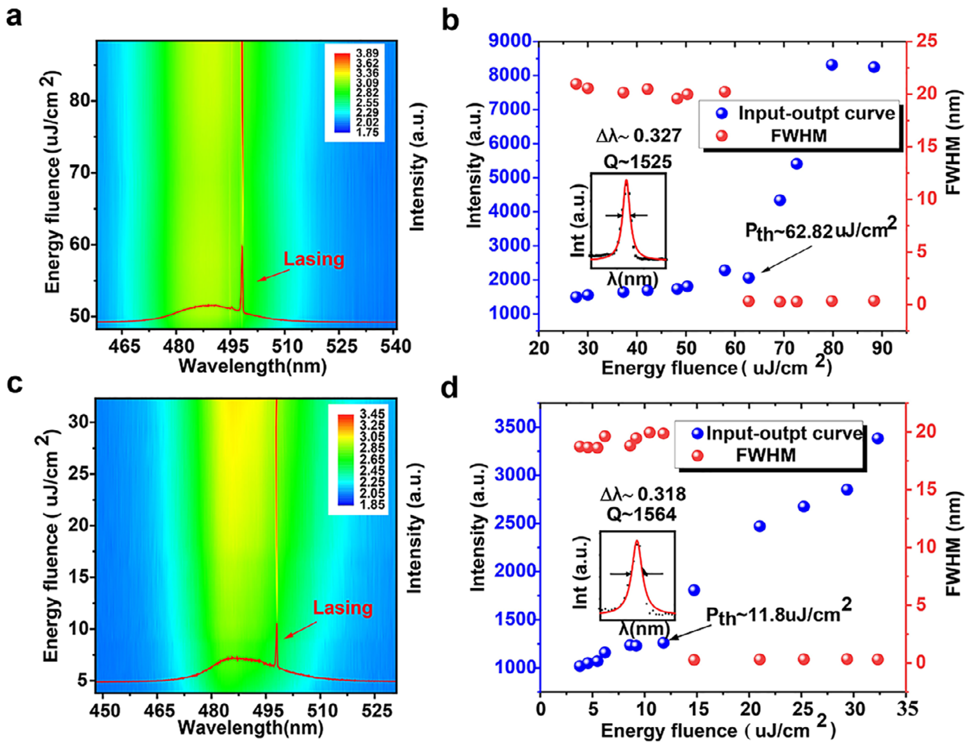

FIGURE 4 | Lasing threshold reduction of a single $CsPbCl_xBr_{3-x}$ perovskite laser. (a,c) 2D color maps of the laser spectra of a single $CsPbCl_xBr_{3-x}$ perovskite laser before and after high-temperature annealing under different energy fluxes, with a center wavelength of 498 nm. (b,d) Dependence of emission intensity and full-width at half-maximum (FWHM) on energy flux before and after annealing (Insets: magnified images of the laser mode fitted with a Lorentzian function).

in defect state density suppresses non-radiative recombination processes, improving carrier lifetime and luminescence efficiency. At the same time, the broadening effect of the PL peak in the annealed samples is reduced, suggesting that the enhancement in crystal uniformity and the improvement in local strain further stabilize the excitons (Figure S6). These findings indicate that high-temperature annealing not only optimizes the optical uniformity of the material but also enhances the photoluminescence stability and intensity by tuning defect states and carrier dynamics, providing important physical support for the design of low-threshold, high-efficiency perovskite lasers.

The $CsPbCl_xBr_{3-x}$ perovskite micro-wires, after high-temperature annealing treatment, provide a natural resonator and gain medium with enhanced photoluminescence, which is ideal for constructing low-threshold, high-performance photonic devices. As shown in Figure 4a,c, the laser performance of a single $CsPbCl_xBr_{3-x}$ perovskite micro-wire is characterized by a confocal μ-PL system equipped with a 405 nm femtosecond pulse laser (190 fs, 6 kHz) and a 1200 g/mm optical multi-channel spectrometer. The 2D color maps show the laser spectra of the micro-wire before and after annealing under different energy fluxes. After annealing, the lasing threshold of the $CsPbCl_xBr_{3-x}$ perovskite micro-wire significantly decreases, and the single lasing peak stabilizes at 498 nm, indicating that the high-temperature annealing effectively enhances the optical gain of the material and optimizes its optical cavity properties. The impact of the anion-position-driven lattice engineering strategy on the lasing performance is quantitatively reflected in the evolution of key emission parameters. Following the annealing process, the lasing threshold of the single $CsPbCl_xBr_{3-x}$ microwire exhibits a dramatic reduction from 62.82 to 11.8 μJ/cm^2 (as shown in Figure 4b,d), while the emission intensity increases by two to three orders of magnitude. Although the quality factor (Q) shows a minor variation from 1525 to 1564-primarily limited by the cavity geometry and spectrometer resolution-the FWHM at the threshold narrows from 0.33 to 0.32 nm, indicating a significant optimization of the optical gain medium. Insets show magnified images of the laser mode fitted with a Lorentzian function, further verifying the improved mode quality. This intrinsic lattice reconfiguration, driven by the relocation of anions from interstitial sites back to regular lattice positions, effectively reduces non-radiative recombination centers. Consequently, the annealing -treated microwires not only provide a high-quality natural resonator but also serve as a superior gain medium with a substantially lowered threshold, laying a solid foundation for further applications in perovskite-based photonics.

In this study, $CsPbCl_xBr_{3-x}$ perovskite microcrystals synthesized via a vapor-phase halide exchange method exhibited remarkable optoelectronic performance after high-temperature annealing. The annealing treatment led to a more than hundredfold enhancement in photoluminescence (PL) intensity, indicating a substantial reduction in internal defects and a significant improvement in radiative recombination efficiency. This enhancement is attributed to improved crystallinity (as shown in Figure S7), lattice strain relaxation, and effective passivation of surface defects. To verify the reproducibility and rule out any experimental contingency, multiple samples were fabricated and tested, all of which exhibited consistent results. Detailed data for these samples are summarized in Table S1.

Importantly, optimized annealing also significantly reduced the lasing threshold of the $CsPbCl_xBr_{3-x}$ microcrystals. This improvement is likely due to the synergistic effect of enhanced optical gain and the optimization of the intrinsic optical cavity structure within the microcrystals. In these cavities, photons are strongly confined, which not only increases laser output efficiency but also lowers the excitation energy required for lasing. Notably, the annealed microcrystals exhibited a high laser quality factor of approximately 1564, indicating minimal optical losses and strong photon confinement. These results highlight the potential of $CsPbCl_xBr_{3-x}$ microcrystals as high-performance gain media for photonic applications, and demonstrate that high-temperature annealing is an effective strategy for tuning and enhancing perovskite laser performance. Table S2 provides a detailed performance benchmark against other reported halide perovskite micro/nano-lasers. The comparison underscores the superior optical properties and low-threshold characteristics achieved in this study, which rank among the highest levels reported to date for alloyed perovskite systems.

3 | Conclusion

In summary, we have established an anion-position-driven lattice reconfiguration strategy to resolve the inherent defect challenges in $CsPbCl_xBr_{3-x}$ perovskite microcrystals synthesized via halide exchange. Our findings reveal that the enhancement in optical performance transcends mere morphological optimization; rather, it is rooted in the transition of halide anions from unstable interstitial sites back to their thermodynamically stable lattice positions. This intrinsic atomic reconfiguration leads to a 2–3 order of magnitude increase in photoluminescence intensity and a nearly three-fold enhancement in exciton binding energy, as confirmed by both temperature-dependent PL and First-principles calculations. The resulting microcrystals exhibit superior lasing characteristics, including a significantly low threshold and an effective quality factor of ~1564. By identifying anion occupancy as a critical descriptor for optical gain in perovskite alloys, this work provides a conceptual breakthrough that distinguishes intrinsic lattice engineering from extrinsic quality improvement. Our approach offers a robust and universal route for developing high-efficiency, low-threshold perovskite micro-lasers and advanced photonic integration.

4 | Experimental Section

4.1 | Synthesis of $CsPbBr_3$ Perovskite Microwires and Halogen Exchange Process

$CsPbBr_3$ perovskite microwires were synthesized using an anti-solvent method consistent with previously reported procedures [39]. The microwires were transferred to a clean glass slide for subsequent treatment using a micro-manipulation system. The glass slide with microwires was placed into a sealed glass petri dish (130 mm in diameter, 25 mm in height), containing 20 g of anhydrous calcium chloride as a desiccant. For halogen exchange, 20 µL of concentrated 37 wt.% hydrochloric acid (HCl) solution was drawn into a pipette, and the wider end of the pipette was sealed. The pipette was then placed into the petri dish. The entire petri dish was tightly wrapped with plastic film to create a sealed environment. The closed petri dish was placed in a 65°C blast drying oven for a reaction time of 7 h. After the reaction, a single halogenated perovskite microwire ($CsPbCl_xBr_{3-x}$) was obtained for subsequent annealing and characterization.

4.2 | Annealing Process of $CsPbCl_xBr_{3-x}$ Alloy Microwires

The synthesized single $CsPbCl_xBr_{3-x}$ alloy perovskite microwire, along with the glass slide, was placed into a clean petri dish (130 mm in diameter, 25 mm in height). A smaller petri dish (60 mm in diameter, 10 mm in height) was used to cover the microwire and glass slide to ensure protection during the annealing process. The entire assembly was then placed in a preheated blast drying oven at 180°C for thermal annealing, and the heating was maintained for 3 h. After the annealing process, the enhanced single alloy perovskite microwire was obtained for subsequent characterization and analysis.

4.3 | Morphological, Structural, and Optical Property Characterization

The morphology and composition of the single $CsPbCl_xBr_{3-x}$ perovskite alloy microwires were characterized using a field emission scanning electron microscope (FE-SEM) equipped with an energy-dispersive X-ray spectroscopy (EDS) detector. The structural properties were analyzed using an X-ray diffraction (XRD) analyzer. Photoluminescence (PL) spectra, absorption spectra, and fluorescence imaging were performed using a highly integrated custom micro-area microscopy system. The lasing characteristics were tested with a confocal micro-area fluorescence system, which includes a femtosecond pulse laser (405 nm), a microscope with a 40× objective lens and a Nikon camera, and an optical multi-channel spectrometer with 1200 g/mm. The PL quantum yield was obtained by a photoluminescence spectrometer (FLS1000, Edinburgh).

4.4 | Theoretical Simulations

First-principles calculations were based on density functional theory (DFT) [50, 51] with generalized gradient approximation (GGA) [52, 53] for exchange correlation potential. Perdew–Burke–Ernzerholf (PBE) functional was used for the GGA as implemented in Vienna ab initio simulation package (VASP) [54]. The electron-ion interaction was treated by projector-augmented-wave (PAW) potentials [55] with a planewave-basis cuff of 400 eV. A primitive cell of $CsPbBr_3$ (20 atoms) in the orthorhombic phase (space group *Pnma*) was used [56, 57]. The whole Brillouin zone was sampled by a 7 × 5 × 7 k-point mesh [58, 59]. Lattice constants and atomic coordinates were fully relaxed until the force on each atom was less than 0.001 eV/Å.

Acknowledgements

The authors thank the support of the National Natural Science Foundation of China (Nos. 52572172, 62105035, 52125205, 52250398, U20A20166, 12374257 and 52192614), the Natural Science Foundation of Jiangsu Province (BK20231441) and the Nanjing University of Aeronautics and Astronautics Graduate Student Research and Practice Innovation Program (xcxjh20242102), National key R&D program of China (2021YFB3200300), Natural Science Foundation of Beijing Municipality (222208), the Fundamental Research Funds for the Central Universities (No. NC2025016).

Conflicts of Interest

The authors declare no conflicts of interest.

Data Availability Statement

The data that support the findings of this study are available from the corresponding author upon reasonable request.

References

1. I. L. Braly, D. W. deQuilettes, L. M. Pazos-Outón, et al., "Hybrid Perovskite Films Approaching the Radiative Limit with over 90% Photoluminescence Quantum Efficiency," *Nature Photonics* 12 (2018): 355–361, https://doi.org/10.1038/s41566-018-0154-z.

2. N. Pourdavoud, T. Haeger, A. Mayer, et al., "Room-Temperature Stimulated Emission and Lasing in Recrystallized Cesium Lead Bromide Perovskite Thin Films," *Advanced Materials* 31 (2019): 1903717, https://doi.org/10.1002/adma.201903717.

3. X. He, P. Liu, H. Zhang, Q. Liao, J. Yao, and H. Fu, "Patterning Multicolored Microdisk Laser Arrays of Cesium Lead Halide Perovskite," *Advanced Materials* 29 (2017): 1604510, https://doi.org/10.1002/adma.201604510.

4. M. K. Hossain, P. Guo, W. Qarony, et al., "Controllable Optical Emission Wavelength in All-Inorganic Halide Perovskite Alloy Microplates Grown by Two-step Chemical Vapor Deposition," *Nano Research* 13 (2020): 2939–2949, https://doi.org/10.1007/s12274-020-2951-1.

5. L. Huang, Q. Gao, L. D. Sun, et al., "Composition-Graded Cesium Lead Halide Perovskite Nanowires with Tunable Dual-Color Lasing Performance," *Advanced Materials* 30 (2018): 1800596, https://doi.org/10.1002/adma.201800596.

6. J. Li, J. Xu, Y. Bao, et al., "Anion-Exchange Driven Phase Transition in $CsPbI_3$ Nanowires for Fabricating Epitaxial Perovskite Heterojunctions," *Advanced Materials* 34 (2022): 2109867, https://doi.org/10.1002/adma.202109867.

7. J. Lu, X. He, F. Li, et al., "Composition-Graded Perovskite Microwire Toward Broad Wavelength Tunable Single-Mode Lasing," *Laser & Photonics Reviews* 18 (2024): 2400555.

8. A. Schleusener, M. Faraji, M. Borreani, et al., "Heterostructures via a Solution-Based Anion Exchange in Microcrystalline 2D Layered Metal-Halide Perovskites," *Advanced Materials* 36 (2024): 2402924, https://doi.org/10.1002/adma.202402924.

9. B. Tang, Y. Hu, J. Lu, et al., "Energy Transfer and Wavelength Tunable Lasing of Single Perovskite Alloy Nanowire," *Nano Energy* 71 (2020): 104641, https://doi.org/10.1016/j.nanoen.2020.104641.

10. X. Wang, M. Shoaib, X. Wang, et al., "High-Quality in-Plane Aligned $CsPbX_3$ Perovskite Nanowire Lasers with Composition-Dependent Strong Exciton–Photon Coupling," *ACS Nano* 12 (2018): 6170–6178, https://doi.org/10.1021/acsnano.8b02793.

11. T. Chen, W. L. Chen, B. J. Foley, et al., "Origin of Long Lifetime of Band-Edge Charge Carriers in Organic–inorganic Lead Iodide Perovskites," *Proceedings of the National Academy of Sciences* 114 (2017): 7519–7524, https://doi.org/10.1073/pnas.1704421114.

12. N. Varnakavi, J. L. Velpugonda, N. Lee, S. Nah, and L. Y. Lin, "In Situ Synthesis of Br-Rich $CsPbBr_3$ Nanoplatelets: Enhanced Stability and High PLQY for Wide Color Gamut Displays," *Advanced Functional Materials* 35 (2024): 2413320, https://doi.org/10.1002/adfm.202413320.

13. M. Li, Y. Yang, Z. Kuang, et al., "Acceleration of Radiative Recombination for Efficient Perovskite LEDs," *Nature* 630 (2024): 631–635, https://doi.org/10.1038/s41586-024-07460-7.

14. K. Wei, T. Zhou, Y. Jiang, et al., "Perovskite Heteroepitaxy for High-Efficiency and Stable Pure-Red LEDs," *Nature* 638 (2025): 949–956, https://doi.org/10.1038/s41586-024-08503-9.

15. Y. Wang, F. Jia, X. Li, S. Teale, P. Xia, and Y. Liu, "Self-Assembled Monolayer–Based Blue Perovskite LEDs," *Science Advances* 9 (2023): adh2140.

16. D. Zhang, Y. Fu, W. Wu, et al., "Comprehensive Passivation for High-Performance Quasi-2D Perovskite LEDs," *Small* 19 (2023): 2206927.

17. N. Kurahashi, M. Runkel, C. Kreusel, et al., "Distributed Feedback Lasing in Thermally Imprinted Phase-Stabilized $CsPbI_3$ Thin Films," *Advanced Functional Materials* 34 (2024): 2405976, https://doi.org/10.1002/adfm.202405976.

18. S. D. Stranks and H. J. Snaith, "Metal-Halide Perovskites for Photovoltaic and Light-Emitting Devices," *Nature Nanotechnology* 10 (2015): 391–402.

19. B. Han, M. Jiang, C. Lin, M. Liu, D. Shi, and C. Kan, "Flexible $CsPbBr_3$ Microwire Photodetector with a Performance Enhanced by Covering It with an Ag Nanolayer," *CrystEngComm* 24 (2022): 7620–7631.

20. J. Li, J. Li, M. An, et al., "Ultralong Compositional Gradient Perovskite Nanowires Fabricated by Source-Limiting Anion Exchange," *ACS Nano* 18 (2024): 30978–30986, https://doi.org/10.1021/acsnano.4c06676.

21. C. Lin, P. Wan, B. Yang, D. Shi, C. Kan, and M. Jiang, "Plasmon-Enhanced Photoresponse and Stability of a $CsPbBr_3$ Microwire/GaN Heterojunction Photodetector With Surface-Modified Ag Nanoparticles," *Journal of Materials Chemistry C* 11 (2023): 12968–12980, https://doi.org/10.1039/D3TC02240D.

22. X. Mo, X. Li, G. Dai, et al., "All-Inorganic Perovskite $CsPbBr_3$ Microstructures Growth via Chemical Vapor Deposition for High-Performance Photodetectors," *Nanoscale* 11 (2019): 21386–21393, https://doi.org/10.1039/C9NR06682A.

23. X. Pan, T. An, J. Sun, et al., "Thermodynamically Induced Crystal Restructuring to Make $CsPbCl_3$ Single Crystal Films for Weak Light Detection," *Nano Research* 17 (2024): 9775–9783, https://doi.org/10.1007/s12274-024-6967-9.

24. L. Sun, J. Li, J. Han, M. Meng, B. Li, and M. Jiang, "High-Sensitivity Self-Powered Photodetector Based on an In Situ Prepared $CsPbBr_3$ Microwire/InGaN Heterojunction," *Optics Express* 31 (2023): 38744, https://doi.org/10.1364/OE.505800.

25. Y. Yang, F. Gao, Q. Liu, et al., "Long and Ultrastable All-Inorganic Single-Crystal $CsPbBr_3$ Microwires: One-Step Solution in-Plane Self-Assembly at Low Temperature and Application for High-Performance Photodetectors," *The Journal of Physical Chemistry Letters* 11 (2020): 7224–7231, https://doi.org/10.1021/acs.jpclett.0c01920.

26. H. Zhou, Z. Song, C. R. Grice, et al., "Self-Powered $CsPbBr_3$ Nanowire Photodetector With a Vertical Structure," *Nano Energy* 53 (2018): 880–886, https://doi.org/10.1016/j.nanoen.2018.09.040.

27. W. Wu, C. Wang, S. Han, and C. Pan, "Recent Advances in Imaging Devices: Image Sensors and Neuromorphic Vision Sensors," *Rare Metals* 43 (2024): 5487–5515, https://doi.org/10.1007/s12598-024-02811-9.

28. Z. Yang, S. Huo, Z. Zhang, et al., "High-Precision Multibit Opto-Electronic Synapses Based on ReS_2 /h-BN/Graphene Heterostructure for Energy-Efficient and High-Accuracy Neuromorphic Computing," *Advanced Functional Materials* 35 (2025): 2509119, https://doi.org/10.1002/adfm.202509119.

29. N. N. Lal, Y. Dkhissi, W. Li, Q. Hou, Y. B. Cheng, and U. Bach, "Perovskite Tandem Solar Cells," *Advanced Energy Materials* 7 (2017): 1602761.

30. K. Zhang, N. Zhu, M. Zhang, L. Wang, and J. Xing, “Opportunities and Challenges in Perovskite LED Commercialization,” *Journal of Materials Chemistry C* 9 (2021): 3795–3799, https://doi.org/10.1039/D1TC00232E.

31. Y. Wang, X. Li, V. Nalla, H. Zeng, and H. Sun, “Solution-Processed Low Threshold Vertical Cavity Surface Emitting Lasers from all-Inorganic Perovskite Nanocrystals,” *Advanced Functional Materials* 27 (2017): 1605088, https://doi.org/10.1002/adfm.201605088.

32. H. Yu, K. Ren, Q. Wu, et al., “Organic–Inorganic Perovskite Plasmonic Nanowire Lasers with a Low Threshold and a Good Thermal Stability,” *Nanoscale* 8 (2016): 19536–19540, https://doi.org/10.1039/C6NR06891J.

33. L. Yuan, J. Lu, M. Li, et al., “Two-Photon Pumped Wavelength-Tunable Single-Mode Plasmonic Nanolaser With Ultralow Threshold,” *Advanced Functional Materials* 35 (2024): 2413250, https://doi.org/10.1002/adfm.202413250.

34. L. Zhang, Y. Wang, A. Chu, et al., “Facet-selective Growth of Halide Perovskite/2D Semiconductor van der Waals Heterostructures for Improved Optical Gain and Lasing,” *Nature Communications* 15 (2024): 5484, https://doi.org/10.1038/s41467-024-49364-0.

35. N. Pourdavoud, S. Wang, A. Mayer, et al., “Photonic Nanostructures Patterned by Thermal Nanoimprint Directly into Organo-Metal Halide Perovskites,” *Advanced Materials* 29 (2017): 1605003, https://doi.org/10.1002/adma.201605003.

36. D. Wen, P. Chen, Y. Liang, X. Mo, and C. Pan, “Regulated Polarization Degree of Upconversion Luminescence and Multiple Anti-Counterfeit Applications,” *Rare Metals* 43 (2024): 2172–2183, https://doi.org/10.1007/s12598-024-02675-z.

37. J. He, S. Wang, R. Han, et al., “Wide Detection Range Flexible Pressure Sensors Based on 3D Interlocking Structure TPU/ZnO NWs,” *Advanced Functional Materials* 35 (2024): 2418791, https://doi.org/10.1002/adfm.202418791.

38. M. Lai, A. Obliger, D. Lu, et al., “Intrinsic Anion Diffusivity in Lead Halide Perovskites Is Facilitated by a Soft Lattice,” *Proceedings of the National Academy of Sciences* 115 (2018): 11929–11934, https://doi.org/10.1073/pnas.1812718115.

39. F. Li, Z. Yang, M. Jiang, et al., “Wavelength Tunable Single-mode Lasing from Cesium Lead Halide Perovskite Microwires,” *Applied Physics Letters* 118 (2021): 071103, https://doi.org/10.1063/5.0035104.

40. J. Lu, X. He, J. Xu, et al., “Two-Photon Pumped Single-Mode Lasing in $CsPbBr_3$ Perovskite Microwire,” *Advanced Functional Materials* 34 (2023): 2308957, https://doi.org/10.1002/adfm.202308957.

41. J. Xing, X. F. Liu, Q. Zhang, et al., “Vapor Phase Synthesis of Organometal Halide Perovskite Nanowires for Tunable Room-Temperature Nanolasers,” *Nano Letters* 15 (2015): 4571–4577, https://doi.org/10.1021/acs.nanolett.5b01166.

42. Y. Fu, H. Zhu, C. C. Stoumpos, et al., “Broad Wavelength Tunable Robust Lasing from Single-Crystal Nanowires of Cesium Lead Halide Perovskites ($CsPbX_3$, X = Cl, Br, I),” *ACS Nano* 10 (2016): 7963–7972, https://doi.org/10.1021/acsnano.6b03916.

43. Y. An, X. Shen, Y. Zhang, et al., “Color-Tunable Photoluminescence and Whispering Gallery Mode Lasing of Alloyed $CsPbCl_3(1–x)$ Br_{3x} Microstructures,” *Advanced Materials Interfaces* 7 (2020): 1902126, https://doi.org/10.1002/admi.201902126.

44. R. Lin, K. Dong, J. Zhao, et al., “Wavelength-Tunable Microlasers Based on Perovskite Sheets Processed from the Solution Saturation-Controlled Method,” *The Journal of Physical Chemistry C* 128 (2024): 7616–7623, https://doi.org/10.1021/acs.jpcc.4c01149.

45. C. Zhang, J. Duan, F. Qin, C. Xu, W. Wang, and J. Dai, “$CsPbBr_3$ Interconnected Microwire Structure: Temperature-Related Photoluminescence Properties and Its Lasing Action,” *Journal of Materials Chemistry C* 7 (2019): 10454–10459, https://doi.org/10.1039/C9TC02913C.

46. L. Song, Y. Liu, R. Guo, and J. Dai, “Excitonic Optical Properties and Lasing Mode Shifts in Square $CsPbBr_3$ Nanoplate Cavities,” *Journal of Luminescence* 251 (2022): 119182, https://doi.org/10.1016/j.jlumin.2022.119182.

47. V. D’Innocenzo, G. Grancini, M. J. Alcocer, et al., “Excitons Versus Free Charges in Organo-Lead Tri-Halide Perovskites,” *Nature Communications* 5 (2014): 3586, https://doi.org/10.1038/ncomms4586.

48. Z. Zhao, M. Zhong, W. Zhou, et al., “Simultaneous Triplet Exciton–Phonon and Exciton–Photon Photoluminescence in the Individual Weak Confinement $CsPbBr_3$ Micro/Nanowires,” *The Journal of Physical Chemistry C* 123 (2019): 25349–25358, https://doi.org/10.1021/acs.jpcc.9b06643.

49. C. Dong, G. Chen, S. Wang, Z. Yu, W. Ke, and G. Fang, “High-Performance Green Light-Emitting-Diode Enabled by Simultaneous Phase Engineering and Crystallization Regulation,” *Advanced Functional Materials* 35 (2025): 2502662, https://doi.org/10.1002/adfm.202502662.

50. M. Ernzerhof and G. E. Scuseria, “Perspective on "Inhomogeneous Electron Gas",” *Theoretical Chemistry Accounts: Theory, Computation, and Modeling (Theoretica Chimica Acta)* 103 (2000): 259–262, https://doi.org/10.1007/s002149900030.

51. W. Kohn and L. J. Sham, “Self-consistent Equations Including Exchange and Correlation Effects,” *Physical Review* 140 (1965): A1133.

52. J. P. Perdew, K. Burke, and M. Ernzerhof, “Generalized Gradient Approximation Made Simple,” *Physical Review Letters* 77 (1996): 3865–3868, https://doi.org/10.1103/PhysRevLett.77.3865.

53. J. P. Perdew, K. Burke, and M. Ernzerhof, “Generalized Gradient Approximation Made Simple,” *Physical Review Letters* 78 (1997): 1396, https://doi.org/10.1103/PhysRevLett.78.1396.

54. G. Kresse and J. Furthmüller, “Efficient Iterative Schemes for Ab Initio Total-Energy Calculations Using a Plane-Wave Basis Set,” *Physical Review B* 54 (1996): 11169–11186, https://doi.org/10.1103/PhysRevB.54.11169.

55. G. Kresse and D. Joubert, “From Ultrasoft Pseudopotentials to the Projector Augmented-Wave Method,” *Physical Review B* 59 (1999): 1758–1775, https://doi.org/10.1103/PhysRevB.59.1758.

56. S. L. Brunton, J. L. Proctor, and J. N. Kutz, “Discovering Governing Equations from Data by Sparse Identification of Nonlinear Dynamical Systems,” *Proceedings of the National Academy of Sciences* 113 (2016): 3932–3937, https://doi.org/10.1073/pnas.1517384113.

57. C. C. Stoumpos, C. D. Malliakas, J. A. Peters, et al., “Crystal Growth of the Perovskite Semiconductor $CsPbBr_3$: a New Material for High-Energy Radiation Detection,” *Crystal Growth & Design* 13 (2013): 2722–2727, https://doi.org/10.1021/cg400645t.

58. H. J. Monkhorst and J. D. Pack, “Special Points for Brillouin-Zone Integrations,” *Physical Review B* 13 (1976): 5188–5192, https://doi.org/10.1103/PhysRevB.13.5188.

59. J. D. Pack and H. J. Monkhorst, “Special Points for Brillouin-Zone Integrations"—A Reply,” *Physical Review B* 16 (1977): 1748–1749, https://doi.org/10.1103/PhysRevB.16.1748.

Supporting Information

Additional supporting information can be found online in the Supporting Information section.

Supporting File: adfm75688-sup-0001-SuppMat.docx.